Tuning the Electrochemical Properties of Polymeric Cobalt Phthalocyanines for Efficient Water Splitting

Yoonbin Kim,[1,†] Daekyu Kim,[2,†] Jeongyeon Lee,[2] Lawrence Yoon Suk Lee[2,3,] and Dennis K. P. Ng[1,]**

[1] Department of Chemistry, The Chinese University of Hong Kong, Shatin, N.T., Hong Kong SAR, China

[2] Department of Applied Biology and Chemical Technology and the State Key Laboratory of Chemical Biology and Drug Discovery, The Hong Kong Polytechnic University, Hung Hom, Kowloon, Hong Kong SAR, China

[3] Research Institute for Smart Energy, The Hong Kong Polytechnic University, Hung Hom, Kowloon, Hong Kong SAR, China

* Corresponding authors: lawrence.ys.lee@polyu.edu.hk (L. Y. S. Lee); dkpn@cuhk.edu.hk (D. K. P. Ng)

[†] These authors contributed equally to this work.

Keywords: phthalocyanine; organic electrode; polymer coating; electrocatalyst; water splitting

Abstract

Polymeric metal phthalocyanines have a great potential as electrocatalysts, yet their preparation and incorporation on a current collector without losing the activity of metal centers remain a challenge. Herein, we report a new strategy for preparing a series of polymeric cobalt phthalocyanines containing S linkers (***p*CoPc-1**) or SO_2 linkers (***p*CoPc-2**) and their tunable electrochemical properties in promoting electrocatalytic water splitting. The ***p*CoPc-1** and ***p*CoPc-2** coated on various substrates show favorable electrocatalytic activities toward oxygen and hydrogen evolution reactions (OER and HER). Particularly, the ***p*CoPc-1** layer on Co_3O_4 nanosheet arrays exerts a cooperative effect enhancing both the OER and HER performances, and the subsequent phosphorization significantly boosts the HER performance with enhanced hydrophilicity and conductivity. The high permeability and stability reinforcement of the ***p*CoPc-1** layer allow the phosphorization of underlying Co_3O_4 to CoP without degradation (**P@*p*CoPc-1/Co_3O_4|CC**), which exhibits remarkably enhanced OER and HER performances as manifested by low overpotentials of 320 and 120 mV at 10 mA cm^{-2}, respectively. When engaged as a bifunctional electrocatalyst for the overall water splitting, the **P@*p*CoPc-1/Co_3O_4|CC** requires a low cell voltage of 1.672 V at 10 mA cm^{-2} and exhibits stable performance for 12 h, showing long-term durability and mechanical robustness. This study demonstrates the collaborative catalytic role of polymeric macrocyclic compounds that offers versatile tunability and stability for various electrocatalytic reactions.

1. Introduction

As a promising solution for the depletion of chemical fuels and deteriorating environmental problems, electrocatalytic water splitting has drawn enormous attention as a sustainable and environment-friendly route to supply clean energy through oxygen and hydrogen evolution reactions (OER and HER, respectively).[1] To overcome the sluggish reaction kinetics of water-splitting reactions, especially OER, electrocatalysts based on noble metals such as Pt, Ru, and Ir, as well as their oxides, have been identified as the most efficient materials for accelerating the water-splitting process.[2] Despite the high efficiency of noble metal-based electrocatalysts, their scarcity and high cost hinder practical and large-scale applications. It is thus highly imperative to develop efficient, robust, and low-cost electrocatalysts that can substitute those noble metal-based ones.

Considerable effort has been put into the development of bifunctional electrocatalysts, such as transition-metal oxides,[3] sulfides,[4] and selenides,[5] for simultaneously accelerating OER and HER. Cobalt-based materials are one of those dual-active electrocatalysts with relatively low cost and high earth abundance. To enhance the activity of cobalt-based electrocatalysts, their structure was modified using various strategies, including heteroatom doping,[6] facet control,[7] and oxygen vacancy creation.[8] Doping other elements, especially phosphorous and nitrogen, was effective in promoting the catalytic activities of cobalt-based electrocatalysts, which can be achieved by phosphorization or calcination process forming metal phosphides[9] or M–N_4 active sites,[10] respectively. Especially, the Co_3O_4 derived from a zeolitic imidazolate framework-67 (ZIF-67) and its phosphorized products have been reported as efficient electrocatalysts owing to their high surface area and phosphorous doping.[11] However, the unique morphology and stability of ZIF-67 often deteriorate during high-temperature treatments for conversion to Co_3O_4.[12] Until now, fine-

tuning of electrocatalytic activities while preserving the structural/morphologic stability of cobalt-based electrocatalysts remains a great challenge.

Surface modification by organic functional molecules can provide a solution for this problem.[13] As a versatile class of organic functional dyes, metal phthalocyanines (MPcs) have a great potential to be utilized as electrocatalysts owing to their intriguing and tunable optical and electronic properties.[14] In particular, polymerization of MPcs or related analogues such as porphyrins can serve as heterogeneous electrocatalysts that also offer a cooperative effect with M–N_4 active sites.[15] When engaged as electrocatalysts on a substrate, these polymeric organic compounds exhibit good permeation for electrolytes, allowing the additional active sites on the substrate to be accessible for improved catalytic performance. Recently, carbon nanotube (CNT)-supported or self-polymerized CoPc compounds have been reported as the electrocatalysts for enhanced CO_2 and O_2 reductions as well as nitrile sensors, showing notably improved stabilities.[16] The polymeric MPc compounds have also been applied to electrocatalytic OER[17] and HER,[18] but their activities were not competitive. Although Sannegowda *et al.*[17a] have demonstrated highly improved electrocatalytic OER performance by physically mixing self-polymerized CoPc with a noble metal oxide (IrO_2), it deviates from the grand purpose of developing affordable electrocatalysts for large-scale overall water splitting. Organic macrocycles usually possess good adhesion properties on various substrates, yet the coating method for polymeric MPc to prepare an electrode is so far limited to dip-coating, physical mixing, and polymerization onto nanoparticles. Moreover, the tuning of MPc properties by varying the peripheral substituents has been rarely explored in their polymeric systems. It is thus of importance to develop a new strategy of constructing polymeric CoPc-based electrocatalysts with tunable electrochemical properties to enhance water-splitting performance.

Herein, we report the preparation of rationally designed polymeric cobalt phthalocyanines that contain S linkers (***p*CoPc-1**) or SO_2 linkers (***p*CoPc-2**), their tunable electrochemical properties, and application in promoting water-splitting reaction. A new strategy of coating polymeric CoPc onto various substrates including SiO_2 nanoparticles, carbon cloth (CC), and CoO- or Co_3O_4-modified CC was developed to prepare an electrode preserving their morphologies and electrocatalytic activities. The effects of the linkers and the subsequent phosphorization on the electronic structure of resulting electrocatalysts were systematically investigated. Both ***p*CoPc-1** and ***p*CoPc-2** show the capability to improve OER and HER activities. In particular, the ***p*CoPc-1** on Co_3O_4-modified CC exhibits favorable OER performance, and its phosphorized form (**P@*p*CoPc-1/Co_3O_4|CC**) remarkably boosts the electrocatalytic OER and HER activities as manifested by low overpotentials of 320 and 120 mV at the current density of 10 mA cm^{-2}, respectively. The water electrolyzer using **P@*p*CoPc-1/Co_3O_4|CC** as both the cathode and anode delivers a low and stable cell voltage of 1.672 V at the current density of 10 mA cm^{-2} for 12 h.

2. Results and Discussion

The polymerization of metal phthalocyanines (MPcs) and their application toward water splitting are associated with several challenges, such as the high aggregation tendency and high hydrophobicity of the macrocycles. To circumvent these issues, novel polymeric CoPc (***p*CoPc**) with linkers of different electrochemical properties were designed and prepared to be coated on various substrates. Subsequent phosphorization of ***p*CoPc** (**P@*p*CoPc**) allows further tuning of the hydrophilicity and electrochemical properties.[19] **Figure 1a** shows a schematic illustration of the synthetic procedures and chemical structures of ***p*CoPc** that contains either electron-donating thioether linkers (***p*CoPc-1**) or electron-withdrawing sulfonyl linkers (***p*CoPc-2**) and their phosphorized products (**P@*p*CoPc-1** and **P@*p*CoPc-2**). In order to achieve one-step cyclization

of phthalocyanines and their polymerization, dimeric phthalonitriles (**Pn dimer**) were first prepared and characterized with ^{1}H and ^{13}C NMR spectroscopy and mass spectrometry (see Experimental Section and **Figures S1** and **S2** in the Supporting Information). Propanedithiol was chosen as a linker to synthesize **Pn dimer-1** containing two thioether (S) groups, and to impart different electrochemical properties to resulting ***p*CoPc**, the **Pn dimer-1** was oxidized to yield **Pn dimer-2**, which has two sulfonyl (SO_2) groups. Due to the different electronic nature of the substituents, the reaction conditions for ***p*CoPc-1** and ***p*CoPc-2** were optimized separately. The ***p*CoPc-1** was synthesized by base-promoted cyclization using 1,8-diazabicyclo[5.4.0]undec-7-ene in a mixed solvent of 1-pentanol and *N*, *N*-dimethylformamide (DMF), while the ***p*CoPc-2** was synthesized by base-free cyclization in a mixed solvent of 1,2-dichlorobenzene (DCB) and DMF. An appropriate amount of DMF was added into 1-pentanol or DCB to enhance the solubility of the precursors and yield a uniform coating of ***p*CoPc** onto the substrates.

Two methods were engaged to prepare the ***p*CoPc** coatings on different types of substrates, namely SiO_2 nanoparticles, bare carbon cloth (CC), and CoO- or Co_3O_4-modified CC under two different reaction conditions: 1) a conventional method in a Schlenk tube with vigorous stirring and 2) a solvothermal method in a Teflon-lined autoclave without stirring. In the presence of substrates, the conventional method enables fine coating of ***p*CoPc** on SiO_2 nanoparticles as shown in **Figure S3a**, while the solvothermal method produces a fiber-like ***p*CoPc** network randomly grown on the surface of SiO_2 (**Figure S3b**). On the other hand, the solvothermal method affords better results on bulkier substrates such as CoO-modified CC, which are difficult to be coated *via* the conventional method due to physical restrictions (**Figure S3c**). Raman spectra confirm the successful ***p*CoPc** coatings by the solvothermal method (**Figure S3d**). Meanwhile, without any substrate, the conventional method yields layers of spherical polymeric particles (**Figure S4a**), whereas the solvothermal method produces entangled fiber-like polymers (**Figure S4b**). With the

aim of enhancing the catalytic performance, the resulting self-polymerized compounds were phosphorized by annealing them at 300 °C in the presence of sodium hypophosphite. Thermalgravimetric analysis (TGA, **Figure S5a**) indicates that the ***p*CoPc** can withstand decomposition at the annealing temperature. Energy dispersive spectroscopic (EDS) mapping images (**Figures 1b** and **1c**) confirm that the phosphorization of ***p*CoPc-1** obtained by both methods yields **P@*p*CoPc-1** of the same elemental composition without changing their morphologies. The P elements are well dispersed on **P@*p*CoPc-1**, which indicates that the high porosity of ***p*CoPc-1** allows good permeation of phosphine gas to reach the entire sample. Brunauer–Emmett–Teller (BET) analyses of ***p*CoPc-1** and ***p*CoPc-2** indicate the specific surface areas of 77.3 and 75.3 $m^2\ g^{-1}$, mean pore diameters of 60.9 and 59.1 nm, and total pore volumes of 1.2 and 1.1 $cm^3\ g^{-1}$, respectively (**Figure S6** and **Table S1**). Despite the different cyclization conditions used, **P@*p*CoPc-2** displays similar microscopic and porosity features (**Figure S7**).

The as-prepared ***p*CoPc**s were further characterized by various spectroscopic methods. The formation of phthalocyanine macrocycles is confirmed by Fourier-transform infrared (FT-IR) spectra shown in **Figure 2a**. The skeletal vibrations of the phthalocyanine core are evident from all samples in the range of 400 – 1,800 cm^{-1}, which are correlated to C=C (1,700 cm^{-1}), C–C (1,600 and 1,520 cm^{-1}), C–H (1,100 and 1,040 cm^{-1}), and Co–N (830 cm^{-1}) vibrations. Also, the distinctive asymmetric and symmetric S=O stretches at 1,300 and 1,145 cm^{-1}, respectively, indicates the presence of sulfonyl linkers in ***p*CoPc-2** and **P@*p*CoPc-2**. The similar spectral features of these two polymeric materials suggest that the macrocyclic skeleton is unchanged during phosphorization. In addition to the FT-IR spectra, the UV–vis spectra of these materials in DMF also show the MPcs' characteristic Q-band (**Figure 2b**). Owing to the substituent effect, the Q-bands of ***p*CoPc-1** and **P@*p*CoPc-1** containing the electron-donating S linkers are red-shifted to 702 nm, while those of ***p*CoPc-2** and **P@*p*CoPc-2** with the electron-withdrawing SO_2 linkers

are found at 690 nm. Moreover, the comparison of the Q-band and B-band (300 – 350 nm) intensities can reveal the degree of polymerization of ***p*CoPc**.[20] The suppressed intensity of the Q-band compared with that of the B-band confirms the successful polymerization of both materials. Notably, the Q-bands are unchanged after the phosphorization, implying no significant changes are made to the π-skeleton. The substituent effects were also detected by Raman spectroscopic analysis (**Figures S5b** and **2c**). The A_{1g} and B_{1g} bands of ***p*CoPc-1** and **P@*p*CoPc-1** are blue-shifted by *ca*. 11 and 3 cm^{-1} compared with those of ***p*CoPc-2** and **P@*p*CoPc-2**, respectively, with the other characteristic signals of MPcs remaining unchanged.[16a]

The surface electronic states and elemental compositions of these materials were further probed by X-ray photoelectron spectroscopy (XPS). The XPS spectra of ***p*CoPc-1** and ***p*CoPc-2** displayed in **Figure S8** reveal the presence of all elements therein. P elemental signals appear only in the phosphorized samples and the strong O signals are mainly due to the oxidation by inevitable air exposure.[21] The high-resolution N 1s spectra of **P@*p*CoPc**'s can be deconvoluted into two peaks, N1 and N2, which correspond to the bridging N and pyrrolic N bonds of MPcs, respectively (**Figure 2d**).[22] The N1 and N2 peaks of **P@*p*CoPc-1** are located at the binding energies of 398.2 and 399.7 eV, while those of **P@*p*CoPc-2** are shifted to 398.6 and 400.2 eV, respectively. The high-resolution C 1s spectrum of **P@*p*CoPc-1** displays four deconvoluted peaks that are assigned to C–C (284.2 eV, C1), C–N (284.8 eV, C2), C=N (285.9 eV, C3), and C–S bonds (288.0 eV, C4, **Figure S9a**).[23] The corresponding C 1s peaks of **P@*p*CoPc-2** are shifted to the higher binding energies by 0.4, 0.5, 0.3, and 0.8 eV, respectively. It is worth noting that the C–S peak is shifted the most, which indicates that such consistent peak shifts observed in the N 1s and C 1s regions of **P@*p*CoPc-2** are related to the replacement of S with SO_2 linkers. The similar yet smaller shifts of N 1s and C 1s peaks are also observed from the samples before phosphorization (**Figures S9b** and

S9c). It is believed that the phosphorization of ***p*CoPc**s augments the substituent effects on their XPS peaks.

Figure 2e compares the high-resolution S 2p spectra of **P@*p*CoPc-1** and **P@*p*CoPc-2**, which display the most distinctive peak shifts. The S $2p_{3/2}$ and S $2p_{1/2}$ peaks of **P@*p*CoPc-1**, corresponding to C–S–C,[24] are located at the binding energies of 162.9 and 164.1 eV, respectively. These peaks shift to 167.7 and 168.7 eV which correspond to C–SO_2–C in **P@*p*CoPc-2**.[24] Such large shifts of S 2p peaks in **P@*p*CoPc-2** strongly suggest a substituent effect arising from the presence of electron-withdrawing S=O moieties. This remarkable substituent effect is also evident in the S 2p orbitals of pristine ***p*CoPc** samples (**Figure S9d**).

The high-resolution P 2p and Co 2p spectra verify the phosphorization of ***p*CoPc** and its influence on the electronic structure of the Co species. The characteristic peak for the P–O bond appears at 133.2 eV in the P 2p spectra of both **P@*p*CoPc-1** and **P@*p*CoPc-2**, confirming successful phosphorizations (**Figure S9e**). Meanwhile, two Co oxidation states are identified from the **P@*p*CoPc-1** and ***p*CoPc-1** with the two Co $2p_{3/2}$ peaks at 780.8 and 779.7 eV corresponding to Co^{2+} and Co^{3+}, respectively[25] (**Figure 2f**). The calculated Co^{2+}/Co^{3+} ratio of **P@*p*CoPc-1** (11.2) is larger than that of ***p*CoPc-1** (1.1) due to the reductive effect of phosphorization (**Table S2**). The same trend is observed from the Co 2p spectra of **P@*p*CoPc-2** and ***p*CoPc-2** (**Figure S9f** and **Table S3**). It is noteworthy that the phosphorization extensively reduces the oxidation state of Co, but the organic nature of the ***p*CoPc** prevents its further reduction to metallic Co^0 species, which is commonly observed for other cobalt oxides.[26] This is consistent with the previous FT-IR results that the molecular structure of ***p*CoPc** is retained during the phosphorization process.

To investigate the tunable electrocatalytic features, the ***p*CoPc** samples were coated on CC by a solvothermal method, phosphorized, and used as electrodes. The SEM images in **Figure S10** reveal uniform and smooth coatings of ***p*CoPc-1** and ***p*CoPc-2** on CC, which show no obvious

morphological changes after the phosphorization as supported by the analyses of the Raman spectra and X-ray diffraction (XRD) patterns (**Figure S11**). Due to the amorphous nature of ***p*CoPc** and **P@*p*CoPc** samples, only signals from CC are observed, confirming no other phases are formed.

The influence of substituents and subsequent phosphorization of ***p*CoPc** samples on CC (***p*CoPc/CC**) were examined by conducting various electrochemical tests. **Figure 3a** shows the linear sweep voltammograms (LSVs) of the pristine and phosphorized ***p*CoPc** samples in the OER region. The ***p*CoPc-1/CC** requires an overpotential (η) of 382 mV to reach a current density of 10 mA cm^{-2}, which is lower than that of ***p*CoPc-2/CC** (412 mV). The favorable OER activity of ***p*CoPc-1/CC** can be ascribed to the electron-donating S linkers that make the 3d orbital of Co metal center partially electron-rich so as to facilitate the formation of OOH* adsorbate on the Co surface, thereby enhancing the OER activity.[27] The subsequent phosphorization further improves the OER activities of both ***p*CoPc-1/CC** and ***p*CoPc-2/CC** as demonstrated by the lowered overpotentials of 368 and 375 mV at 10 mA cm^{-2}, respectively. As suggested by XPS analysis (**Figure 2f**), the phosphorization of ***p*CoPc** samples reduces the surface oxidation state of the Co centers, shifting the majority of Co species to Co^{2+} state. The high-spin Co^{2+} state was reported to show better OER activity than the low-spin Co^{3+} species.[25, 28] Furthermore, the phosphorization process is known to improve the electrical conductivity and hydrophilicity, both of which contribute to the enhanced electrocatalytic performance.[19, 29] The Tafel plots presented in **Figure 3b** reveal the enhanced catalytic kinetics of **P@*p*CoPc-1/CC** with the lowest Tafel slope of 102.9 mV dec^{-1} compared with those of ***p*CoPc-1/CC** (147 mV dec^{-1}), ***p*CoPc-2/CC** (235 mV dec^{-1}), and **P@*p*CoPc-2/CC** (131.4 mV dec^{-1}). Electrochemical impedance spectroscopic (EIS) measurements indicate that the **P@*p*CoPc-1/CC** possesses the lowest charge transfer resistance

(R_{ct}) of 6.16 Ω among all the samples investigated, which clearly illustrates the benefits of the S linkers and phosphorization (**Figure 3c** and **Table S3**).

Interestingly, an opposite trend of catalytic activity is observed in the HER region. The ***p*CoPc-2/CC** shows better HER catalytic activity with an overpotential of 461 mV at 10 mA cm^{-2} compared with ***p*CoPc-1/CC** (480 mV, **Figure 3d**). This can be explained with the electron-withdrawing SO_2 linkers in ***p*CoPc-2**, which endow the Co center with more reducing power and thereby shifting the water reduction potential positively, lowering the overpotential of HER.[30] The HER activities of ***p*CoPc-1/CC** and ***p*CoPc-2/CC** are also enhanced by the phosphorization, and **P@*p*CoPc-1/CC** and **P@*p*CoP-2/CC** display overpotentials of 428 and 418 mV to reach a current density of 10 mA cm^{-2}, respectively. In addition to the improved conductivity and hydrophilicity, P atom is well known to act as a proton acceptor and facilitate the HER process.[31] The corresponding Tafel plots (**Figure 3e**) display the lowest slope of **P@*p*CoPc-2/CC** (157.6 mV dec^{-1}) followed by **P@*p*CoPc-1/CC** (167.6 mV dec^{-1}), ***p*CoPc-2/CC** (191.0 mV dec^{-1}), and ***p*CoPc-1/CC** (225.9 mV dec^{-1}), which confirms the enhanced HER kinetics by phosphorization. Similarly, the EIS spectra obtained under HER conditions indicate the smallest R_{ct} of **P@*p*CoPc-2/CC** (15.05 Ω) among all the samples (**Figure 3f** and **Table S3**). In the stability tests under electrocatalytic conditions for OER and HER, the **P@*p*CoPc-1/CC** and **P@*p*CoPc-2/CC** exhibit the most stable performances, respectively, without significant degradation in a period of 20 h (**Figure S12**). The electrocatalytic OER and HER performances of ***p*CoPc**-based electrodes can be rationally tuned and enhanced by selecting suitable linkers and phosphorization.

Our coating strategy for ***p*CoPc** was further engaged to prepare bifunctional overall water-splitting electrocatalysts using two-dimensional (2D) Co_3O_4 nanosheet arrays on CC as a substrate. The 2D Co_3O_4 nanosheet arrays can offer a large surface area that can be easily phosphorized.[32] With the permeable ***p*CoPc** layers coated, the 2D Co_3O_4 nanosheet arrays are anticipated to play a

role in boosting electrocatalytic water splitting performance by exerting cooperative catalytic effects. The 2D Co_3O_4 nanosheet arrays on CC (denoted as **Co_3O_4|CC**) were prepared by directly growing the zeolitic imidazolate framework-67 (ZIF-67) on CC and annealing them at a high temperature in the air. The ***p*CoPc-1** was selected as a coating layer based on its superior OER and comparable HER activities in the previous results. The ***p*CoPc-1**-coated 2D Co_3O_4 nanosheet arrays on CC (***p*CoPc-1/Co_3O_4|CC**) were fabricated by a solvothermal method and subsequently phosphorized (**P@*p*CoPc-1/Co_3O_4|CC**) in a similar fashion to those on bare CC (**Figure S13**).

Figures 4a and **4b** are the SEM images of ***p*CoPc-1/Co_3O_4|CC** and its phosphorized product, respectively, which show that the spiky nanosheet array morphology of Co_3O_4 is well retained. The phosphorization of bare Co_3O_4 on CC (**P@Co_3O_4|CC**), on the contrary, removes the majority of Co_3O_4 structures, exposing the underlying CC (**Figure S13**). Owing to the ***p*CoPc-1** coating that acts as a protective layer, the structural collapse and detachment of Co_3O_4 nanosheets from CC are prevented during the phosphorization process. Raman spectra of ***p*CoPc-1/Co_3O_4|CC** and **P@*p*CoPc-1/Co_3O_4|CC** identify no noticeable changes after the phosphorization (**Figure S14a**). The ***p*CoPc-1/Co_3O_4|CC** exhibits an XRD pattern similar to that of ***p*CoPc-1/CC** except for the (311) signal from Co_3O_4 (**Figure S14b**). The XRD pattern of the **P@*p*CoPc-1/Co_3O_4|CC** displays two additional small peaks at 31.8 and 48.2° attributed to the (011) and (211) planes of cobalt phosphide (CoP, JCPDS no. 29-0497), implying a partial phosphorization of Co_3O_4 substrate owing to the permeable nature of ***p*CoPc-1** allowing phosphine gas to penetrate and react with the Co_3O_4. The TEM image of a single **P@*p*CoPc-1/Co_3O_4|CC** flake displays numerous nanoparticles (average d = 6.5 nm) coated with a thin layer (**Figure 4c**). The lattice fringes with a *d*-spacing of 0.283 nm are evident in the high-resolution TEM (HRTEM) image of the nanoparticle (**Figure 4d**), which corresponds to the (011) plane of CoP.[33] EDS mapping images presented in **Figure**

4e clearly unveil the CoP core region with dense Co and P elements as well as the **P@*p*CoPc** coating layer.

The changes in surface electronic states and elemental compositions of ***p*CoPc-1/Co$_3$O$_4$|CC** after phosphorization were probed by XPS analysis. The survey XPS spectra in **Figure S15** confirm the presence of all the elements in ***p*CoPc-1**, **P@*p*CoPc-1**, and **Co$_3$O$_4$**. Upon the phosphorization of ***p*CoPc-1/Co$_3$O$_4$|CC**, high-resolution O 1s spectra given in **Figure 4f** disclose the disappearance of Co–O peak at 529.1 eV with a concomitant appearance of evident P=O peak at 532.9 eV, which confirms the transformation of Co_3O_4 to CoP. It is also supported by a strong P–O peak at 133.8 eV in the high-resolution P 2p spectrum of **P@*p*CoPc-1/Co$_3$O$_4$|CC** (**Figure 4g**), which arises from the surface oxidation of CoP.[34] Meanwhile, the high-resolution Co $2p_{3/2}$ spectra (**Figure 4h**) indicates that all Co^{3+} species (779.7 eV) in ***p*CoPc-1/Co$_3$O$_4$|CC** are reduced mostly to Co^{2+} (781.3 eV) and minor metallic Co^0 species (778.1 eV) during the phosphorization. The bifunctional electrocatalytic properties of these electrocatalysts were evaluated using a three-electrode cell in 1.0 M KOH. **Figure 5a** compares the OER polarization curves of the electrocatalysts, where the **P@*p*CoPc-1/Co$_3$O$_4$|CC** requires the lowest overpotential of 320 mV at a current density of 10 mA cm^{-2}, followed by ***p*CoPc-1/Co$_3$O$_4$|CC** (365 mV), **Co$_3$O$_4$|CC** (370 mV), and **P@Co$_3$O$_4$|CC** (360 mV). Compared with **P@Co$_3$O$_4$|CC**, the **P@*p*CoPc-1/Co$_3$O$_4$|CC** electrode delivers a more stable OER performance in a 12-h chronoamperometric reaction (inset in **Figure 5a**), which demonstrates the contribution of ***p*CoPc-1** layer to the stability. The OER stability of the **P@*p*CoPc-1/Co$_3$O$_4$|CC** electrode was also confirmed by a consecutive cyclic voltammetry (CV) test. **Figure S16a** shows that the **P@*p*CoPc-1/Co$_3$O$_4$|CC** is activated and stabilized in the initial few cycles, showing a steady change of the redox couple at 1.13 – 1.23 V, which is related to the generation of intermediate Co^{3+} species. Although the CVs are scanned at a faster scan rate (50 mV s^{-1}) than for the LSV measurements (2 mV s^{-1}), the **P@*p*CoPc-**

1/Co_3O_4|CC displays stable CV curves for 1,000 cycles with a negligible change in OER current. The corresponding Tafel plots (**Figure 5b**) indicate the smaller Tafel slopes for the phosphorized samples. In particular, the Tafel slope of **P@*p*CoPc-1/Co_3O_4|CC** (57.4 mV dec^{-1}) is considerably reduced from that of ***p*CoPc-1/Co_3O_4|CC** (140 mV dec^{-1}). This indicates the facilitated OER kinetics with a shift of rate-determining step (RDS) from the second step (M–O* formation) to the third step (M–OOH* formation) of OER process,[35] suggesting a collaborative interaction between the outer **P@*p*CoPc-1** and the inner **P@Co_3O_4** on CC. The superior OER performance of **P@*p*CoPc-1/Co_3O_4|CC** is further corroborated by EIS measurements where the **P@*p*CoPc-1/Co_3O_4|CC** shows a remarkably small charge transfer resistance (R_{ct}) of 3.18 Ω compared with the other samples (**Figure 5c** and **Table S5**).

A similar trend was observed for the catalytic HER activity of these electrocatalysts. The LSV curves obtained in the HER region (**Figure 5d**) indicate a superior HER activity of **P@*p*CoPc-1/Co_3O_4|CC** with the lowest overpotential of 120 mV at 10 mA cm^{-2} compared with those of **P@Co_3O_4|CC** (140 mV), ***p*CoPc-1/Co_3O_4|CC** (281 mV), and **Co_3O_4|CC** (311 mV). Similar to the case of OER, the **P@*p*CoPc-1/Co_3O_4|CC** exhibits a more stable HER performance in long-term and consecutive CV tests thanks to the ***p*CoPc-1** layer (inset in **Figure 5d** and **Figure S16b**). The corresponding Tafel slope of **P@*p*CoPc-1/Co_3O_4|CC** (98.4 mV dec^{-1}, **Figure 5e**) is the smallest compared with those of **Co_3O_4|CC** (144.8 mV dec^{-1}), **P@Co_3O_4|CC** (108.7 mV dec^{-1}), and ***p*CoPc-1/Co_3O_4|CC** (172.2 mV dec^{-1}). This also suggests that the **P@*p*CoPc-1/Co_3O_4|CC** follows the Volmer–Heyrovsky mechanism where the RDS is a hydrogen desorption step unlike the other samples (hydrogen adsorption step in Volmer mechanism).[29] EIS spectra shown in **Figure 5f** also reveal that the **P@*p*CoPc-1/Co_3O_4|CC** has the smallest R_{ct} of 5.05 Ω, indicating its favorable charge transfer kinetics during HER (**Table S6**).

Based on the best HER performance of **P@*p*CoPc-2|CC** among the samples prepared on bare CC (**Figure 3d**), it is reasonable to fabricate **P@*p*CoPc-2/Co_3O_4|CC** for testing HER performance. The **P@*p*CoPc-2/Co_3O_4|CC** requires an overpotential of 135 mV at 10 mA cm^{-1}, which outperforms **P@Co_3O_4|CC** but inferior to **P@*p*CoPc-1/Co_3O_4|CC** (**Figure S17a**). When deposited on Co_3O_4-modifed CC, the **P@*p*CoPc-1** performs better than **P@*p*CoPc-2**. **Figure S17b** discloses that the OER activity of **P@*p*CoPc-1/Co_3O_4|CC** is also better than that of **P@*p*CoPc-2/Co_3O_4|CC**, showing a larger performance difference than that between **P@*p*CoPc-1|CC** and **P@*p*CoPc-2|CC** (**Figure 3a**). These results indicate that the substituents effect of the ***p*CoPc** is well manifested when they are directly coated on CC but suppressed by the interaction with **P@Co_3O_4** on CC, which influences the electronic configuration of active centers. For instance, the electron-withdrawing property of sulphonyl groups may be suppressed by the electron-rich metal phosphide substrate. As a control sample, a phosphorized physical mixture of ***p*CoPc-1** and Co_3O_4 nanoparticles, namely **P@(*p*CoPc-1+Co_3O_4)|CC**, was prepared according to the determined loading masses of ***p*CoPc-1** and Co_3O_4 in **P@*p*CoPc-1/Co_3O_4|CC** (**Table S7**). The **P@(*p*CoPc-1+Co_3O_4)|CC** exhibits poor catalytic activities toward both OER and HER (**Figure S18**), which highlights the importance of intimate interaction between **P@*p*CoPc-1** and **P@Co_3O_4** enabled by our coating method.

Electrochemical active surface area (ECSA) is an important criterion in evaluating electrocatalysts, which can be estimated by calculating the double-layer capacitance (C_{dl}) from a series of CVs as shown in **Figure S19**. As compared in **Figure S19f**, the C_{dl} values of **Co_3O_4|CC** (14.2 mF cm^{-2}) and ***p*CoPc-1/Co_3O_4|CC** (13.6 mF cm^{-2}) are largely enhanced after the phosphorization (**P@Co_3O_4|CC**: 35.0 mF cm^{-2}; **P@*p*CoPc-1/Co_3O_4|CC**: 33.9 mF cm^{-2}), which is consistent with the previous reports.[8b, 36] This also suggests that the ***p*CoPc-1** layer is permeable not to hinder the phosphorization of underlying **Co_3O_4** nor the active sites. The C_{dl} of the

P@(*p*CoPc-1+Co_3O_4)|CC is only 18.1 mF cm^{-2}, which reveals the limited number of accessible active sites when prepared by physical mixing.

The durability of **P@*p*CoPc-1/Co_3O_4|CC** was accessed by SEM and XRD analyses after the catalytic reactions. The post-OER SEM image of **P@*p*CoPc-1/Co_3O_4|CC** reveals its well-preserved nanosheet arrays of slightly roughened surface (**Figure S20a**), which suggests the phase transition during OER process. The post-OER XRD pattern shown in **Figure S20c** supports this with two small peaks at 20.1 and 38.8° attributed to the (003) and (012) planes of CoOOH (JCPDS no. 14-0673) as well as the vanished CoP peaks. During HER catalysis, the **P@*p*CoPc-1/Co_3O_4|CC** also retains its morphology as evidenced by the post-HER SEM in **Figure S20b**. The spiky tips of nanosheet are, however, flattened and a few thicker nanoplates are observed, which suggests the surface reconstruction of CoP.[37] This is in good agreement with the post-HER XRD pattern that shows two tiny peaks at 19.1 and 38.0° correlated to the (001) and (011) planes of $Co(OH)_2$ (**Figure S20d**, JCPDS no. 74-1057). The changes in the surface electronic states of **P@*p*CoPc-1/Co_3O_4|CC** after OER and HER were further investigated by conducting XPS analysis. High-resolution Co 2p spectra indicate that Co^0 species disappears in the post-OER and post-HER samples (**Figure 6a**). This is most likely caused by the surface reconstruction during the catalysis in alkaline media.[33, 37] A new peak assigned to Co^{3+} species emerges from the post-OER samples, indicating that some of Co species in **P@*p*CoPc-1/Co_3O_4|CC** are electrochemically transformed to CoOOH species that is known as the real active phase of Co-based material for OER.[33] Meanwhile, no obvious change is observed after HER except for the vanishment of metallic Co^0 species, which coincides with other reports of metallic phosphides.[37-38] These changes in Co species mostly arise from the active participation of CoP species on the inner substrate, while the activity of ***p*CoPc-1** could be observed by the high-resolution S 2p and N 1s spectra. The S $2p_{3/2}$ and S $2p_{1/2}$ peaks for C–S–C bonding are still observed after HER and OER

(**Figure 6b**). Noticeably, a new pair of peaks at 168.7 and 167.4 eV appears after OER, which corresponds to the oxidized sulfur, probably due to the interaction with OER intermediates. The N 1s spectrum of the post-OER **P@*p*CoPc-1/Co$_3$O$_4$|CC** displays a pair of new peaks, corresponding to the partially oxidized N1′ (399.0 eV) and N2′ (400.5 eV, **Figure 6c**), due to the interaction of the bridging N (N1) and pyrrolic N (N2) with oxygen-containing intermediates,[39] whereas that of the post-HER sample remains unchanged. Based on the XPS analyses of the samples after catalysis, it is speculated that the molecular structure of ***p*CoPc-1** remains intact despite of some changes in electronic states, which indicates the stable participation of the ***p*CoPc-1** layer during the catalysis.

Inspired by the favorable OER and HER performances of **P@*p*CoPc-1/Co$_3$O$_4$|CC**, a two-electrode cell was prepared for testing the overall water splitting reaction using the **P@*p*CoPc-1/Co$_3$O$_4$|CC** as both anode and cathode (**P@*p*CoPc-1/Co$_3$O$_4$|CC||P@*p*CoPc-1/Co$_3$O$_4$|CC**, inset in **Figure 6d**). Previous results of individual overpotentials for OER (320 mV) and HER (120 mV) suggest an overall potential of *ca*. 1.67 V for overall water splitting. The **P@*p*CoPc-1/Co$_3$O$_4$|CC** electrodes require an overpotential of 1.672 V to reach 10 mA cm^{-2} (**Figure 6d**) with stable performance for continuous 12-h operation with no significant loss of catalytic activity after 1,000 cycles (**Figure 6e**). As expected, the **P@*p*CoPc-1/Co$_3$O$_4$|CC||P@*p*CoPc-1/Co$_3$O$_4$|CC** outperforms the electrolyzer composed of **P@*p*CoPc-1/Co$_3$O$_4$|CC** and **P@*p*CoPc-2/Co$_3$O$_4$|CC** as the anode and cathode, respectively (**P@*p*CoPC-1/Co$_3$O$_4$|CC||P@*p*CoPC-2/Co$_3$O$_4$|CC**, **Figure 21**). These electrocatalytic performances of **P@*p*CoPc-1/Co$_3$O$_4$|CC** are highly competitive with those of previously reported organic- or inorganic-based electrocatalysts (**Table S8)**. To evaluate the Faradaic efficiency of the water splitting by **P@*p*CoPc-1/Co$_3$O$_4$|CC**, the volumes of H_2 and O_2 evolved were measured by a water–gas displacement method using an H-type cell. The measured and calculated yields of H_2 and O_2 at a current density of 50 mA cm^{-2} are presented in **Figure 6f**.

The ratio between the amount of H_2 and O_2 generated is 2.06, which is close to the theoretical value. The corresponding Faradic efficiencies for HER and OER are calculated as 98.6 and 95.7 %, respectively (see the Faradaic efficiency section in the Supporting Information for details), which suggest a comparable conversion yield from electron to gas species.

3. Conclusion

In summary, a facile strategy to prepare efficient water-splitting electrocatalysts employing ***p*CoPc** as coating layers has been developed. The substituent effect of ***p*CoPc** linkers endowed the ***p*CoPc-1**- and ***p*CoPc-2**-coated electrodes with superior electrocatalytic activities for OER and HER, respectively. Subsequent phosphorization enabled a further enhancement of the electrocatalytic performance of the ***p*CoPc**-modified electrodes without degradation of the morphology. Our coating strategy was further demonstrated for the preparation of a bifunctional electrocatalyst for overall water splitting. The as-prepared **P@*p*CoPc-1/Co_3O_4|CC** electrodes exhibited a significant enhancement in OER and HER performances compared with **P@Co_3O_4|CC** without the **P@*p*CoPc-1** layer. Such improved electrocatalytic performances could be attributed to the structural stability, cooperative catalytic effect, enhanced hydrophilicity and conductivity, and retained active sites of substrates owing to the excellent permeability of ***p*CoPc-1** layer. Furthermore, the water electrolyzer using **P@*p*CoPc-1/Co_3O_4|CC** as both anode and cathode can drive a current density of 10 mA cm^{-2} at a cell voltage of 1.672 V with stable performance for 12 h. This work provides an insight into the rational design of advanced electrocatalysts and opens a new path of tuning the electrocatalytic properties with a collaborative catalytic enhancement for multifunctional electrodes in the fields of energy storage and conversion.

Supporting Information

Supporting Information is available from the Wiley Online Library or from the author.

Acknowledgments

We gratefully acknowledge the financial support from the Innovation and Technology Commission of Hong Kong and The Hong Kong Polytechnic University (1-BE0Y), as well as the Research Grants Council of the Hong Kong Special Administrative Region for a grant (Ref. No. 14324116) and the award of Hong Kong PhD Fellowship to Y.K. and D.K.

Conflict of Interest

The authors declare no conflict of interest.

Received: ((will be filled in by the editorial staff))
Revised: ((will be filled in by the editorial staff))
Published online: ((will be filled in by the editorial staff))

References

[1] a) T. R. Cook, D. K. Dogutan, S. Y. Reece, Y. Surendranath, T. S. Teets, D. G. Nocera, *Chem. Rev.* **2010**, 110, 6474; b) N. S. Lewis, D. G. Nocera, *Proc. Natl. Acad. Sci. USA* **2006**, 103, 15729.

[2] a) S. Cherevko, S. Geiger, O. Kasian, N. Kulyk, J.-P. Grote, A. Savan, B. R. Shrestha, S. Merzlikin, B. Breitbach, A. Ludwig, K. J. J. Mayrhofer, *Catal. Today* **2016**, 262, 170; b) Y. Lee, J. Suntivich, K. J. May, E. E. Perry, Y. Shao-Horn, *J. Phys. Chem. Lett.* **2012**, 3, 399; c) D. Wang, Q. Li, C. Han, Q. Lu, Z. Xing, X. Yang, *Nat. Commun.* **2019**, 10, 3899.

[3] a) S. L. Zhang, B. Y. Guan, X. F. Lu, S. Xi, Y. Du, X. W. Lou, *Adv. Mater.* **2020**, 32, 2002235; b) S. Jung, C. C. L. McCrory, I. M. Ferrer, J. C. Peters, T. F. Jaramillo, *J. Mater. Chem. A* **2016**, 4, 3068.

[4] a) Y. Wu, X. Liu, D. Han, X. Song, L. Shi, Y. Song, S. Niu, Y. Xie, J. Cai, S. Wu, J. Kang, J. Zhou, Z. Chen, X. Zheng, X. Xiao, G. Wang, *Nat. Commun.* **2018**, 9, 1425; b) C. Han, Y. Zhang, P. Gao, S. Chen, X. Liu, Y. Mi, J. Zhang, Y. Ma, W. Jiang, J. Chang, *Nano Lett.* **2017**, 17, 7767; c) Y. Wu, F. Li, W. Chen, Q. Xiang, Y. Ma, H. Zhu, P. Tao, C. Song, W. Shang, T. Deng, J. Wu, *Adv. Mater.* **2018**, 30, 1803151.

[5] a) Z. Fang, L. Peng, Y. Qian, X. Zhang, Y. Xie, J. J. Cha, G. Yu, *J. Am. Chem. Soc.* **2018**, 140, 5241; b) Y. Zhou, J. Zhang, H. Ren, Y. Pan, Y. Yan, F. Sun, X. Wang, S. Wang, J. Zhang, *Appl. Catal. B: Environ.* **2020**, 268, 118467.

[6] X. Zou, J. Su, R. Silva, A. Goswami, B. R. Sathe, T. Asefa, *Chem. Commun.* **2013**, 49, 7522.

[7] Z. Chen, C. X. Kronawitter, B. E. Koel, *Phys. Chem. Chem. Phys.* **2015**, 17, 29387.

[8] a) L. Yang, R. Liu, L. Jiao, *Adv. Funct. Mater.* **2020**, 30, 1909618; b) Z. Xiao, Y. Wang, Y.-C. Huang, Z. Wei, C.-L. Dong, J. Ma, S. Shen, Y. Li, S. Wang, *Energy Environ. Sci* **2017**, 10, 2563.

[9] a) P. Zhang, X. F. Lu, J. Nai, S.-Q. Zang, X. W. Lou, *Adv. Sci.* **2019**, 6, 1900576; b) L. Yang, Z. Guo, J. Huang, Y. Xi, R. Gao, G. Su, W. Wang, L. Cao, B. Dong, *Adv. Mater.* **2017**, 29, 1704574; c) H. Zhou, F. Yu, J. Sun, R. He, S. Chen, C.-W. Chu, Z. Ren, *Proc. Natl. Acad. Sci. USA* **2017**, 114, 5607.

[10] a) L. Fu, Y. Chen, Z. Liu, *J. Mol. Catal. A: Chem.* **2015**, 408, 91; b) T. Marshall-Roth, N. J. Libretto, A. T. Wrobel, K. J. Anderton, M. L. Pegis, N. D. Ricke, T. V. Voorhis, J. T. Miller, Y. Surendranath, *Nat. Commun.* **2020**, 11, 5283.

[11] a) Y. Pan, K. Sun, S. Liu, X. Cao, K. Wu, W.-C. Cheong, Z. Chen, Y. Wang, Y. Li, Y. Liu, D. Wang, Q. Peng, C. Chen, Y. Li, *J. Am. Chem. Soc.* **2018**, 140, 2610; b) X. Li, Q. Jiang, S. Dou, L. Deng, J. Huo, S. Wang, *J. Mater. Chem. A* **2016**, 4, 15836.

[12] a) L. Ji, J. Wang, X. Teng, T. J. Meyer, Z. Chen, *ACS Catal.* **2020**, 10, 412; b) P. Li, H. C. Zeng, *J. Mater. Chem. A* **2018**, 6, 2231.

[13] a) J. Al Cheikh, A. Villagra, A. Ranjbari, A. Pradon, M. Antuch, D. Dragoe, P. Millet, L. Assaud, *Appl. Catal. B: Environ.* **2019**, 250, 292; b) J.-X. Feng, S.-Y. Tong, Y.-X. Tong, G.-R. Li, *J. Am. Chem. Soc.* **2018**, 140, 5118.

[14] a) K. Chen, K. Liu, P. An, H. Li, Y. Lin, J. Hu, C. Jia, J. Fu, H. Li, H. Liu, Z. Lin, W. Li, J. Li, Y.-R. Lu, T.-S. Chan, N. Zhang, M. Liu, *Nat. Commun.* **2020**, 11, 4173; b) D.-D. Ma, S.-G. Han, C. Cao, X. Li, X.-T. Wu, Q.-L. Zhu, *Appl. Catal. B: Environ.* **2020**, 264, 118530; c) Z. Yue, C. Ou, N. Ding, L. Tao, J. Zhao, J. Chen, *ChemCatChem* **2020**, 12, 6103.

[15] a) X. Gao, S. DelaCruz, C. Zhu, S. Cheng, D. Gardner, Y. Xie, C. Carraro, R. Maboudian, *Carbon* **2019**, 148, 64; b) G. Xu, H. Lei, G. Zhou, C. Zhang, L. Xie, W. Zhang, R. Cao, *Chem. Commun.* **2019**, 55, 12647.

[16] a) N. Han, Y. Wang, L. Ma, J. Wen, J. Li, H. Zheng, K. Nie, X. Wang, F. Zhao, Y. Li, J. Fan, J. Zhong, T. Wu, D. J. Miller, J. Lu, S.-T. Lee, Y. Li, *Chem* **2017**, 3, 652; b) S. Aralekallu, I. Mohammed, N. Manjunatha, M. Palanna, Dhanjai, L. K. Sannegowda, *Sens. Actuators B Chem.* **2019**, 282, 417.

[17] a) S. Aralekallu, V. A. Sajjan, M. Palanna, K. Prabhu C P, M. Hojamberdiev, L. K. Sannegowda, *J. Power Sources* **2020**, 449, 227516; b) W.-Z. Cheng, J.-L. Liang, H.-B. Yin, Y.-J. Wang, W.-F. Yan, J.-N. Zhang, *Rare Metals* **2020**, 39, 815; c) B. Öztaş, D. Akyüz, A. Koca, *Phys. Chem. Chem. Phys.* **2017**, 19, 26121; d) D. Qi, X. Chen, W. Liu, C. Liu, W. Liu, K. Wang, J. Jiang, *Inorg. Chem. Front.* **2020**, 7, 642.

[18] a) D. Akyüz, B. Keskin, U. Şahintürk, A. Koca, *Appl. Catal. B: Environ.* **2016**, 188, 217; b) İ. Özçeşmeci, A. Demir, D. Akyüz, A. Koca, A. Gül, *Inorg. Chim. Acta* **2017**, 466, 591.

[19] F. Yu, H. Zhou, Y. Huang, J. Sun, F. Qin, J. Bao, W. A. Goddard, S. Chen, Z. Ren, *Nat. Commun.* **2018**, 9, 2551.

[20] D. Wöhrle, E. Preußner, *Macromol. Chem. Phys* **1985**, 186, 2189.

[21] X. Hu, S. Zhang, J. Sun, L. Yu, X. Qian, R. Hu, Y. Wang, H. Zhao, J. Zhu, *Nano Energy* **2019**, 56, 109.

[22] a) Y. Wang, N. Hu, Z. Zhou, D. Xu, Z. Wang, Z. Yang, H. Wei, E. S.-W. Kong, Y. Zhang, *J. Mater. Chem.* **2011**, 21, 3779; b) Y. Xia, S. Kashtanov, P. Yu, L.-Y. Chang, K. Feng, J. Zhong, J. Guo, X. Sun, *Nano Energy* **2020**, 67, 104163; c) I. S. Kwon, I. H. Kwak, J. Y. Kim, H. G. Abbas, T. T. Debela, J. Seo, M. K. Cho, J.-P. Ahn, J. Park, H. S. Kang, *Nanoscale* **2019**, 11, 14266.

[23] a) W. Gu, M. Sevilla, A. Magasinski, A. B. Fuertes, G. Yushin, *Energy Environ. Sci* **2013**, 6, 2465; b) D. G. d. Oteyza, A. El-Sayed, J. M. Garcia-Lastra, E. Goiri, T. N. Krauss, A. Turak, E. Barrena, H. Dosch, J. Zegenhagen, A. Rubio, Y. Wakayama, J. E. Ortega, *J. Chem. Phys.* **2010**, 133, 214703; c) M. Wang, J. Han, Y. Hu, R. Guo, *RSC Adv.* **2017**, 7, 15513.

[24] L. Qie, W. Chen, X. Xiong, C. Hu, F. Zou, P. Hu, Y. Huang, *Adv. Sci.* **2015**, 2, 1500195.

[25] L. Xu, Q. Jiang, Z. Xiao, X. Li, J. Huo, S. Wang, L. Dai, *Angew. Chem. Int. Ed.* **2016**, 55, 5277.

[26] a) Y. Men, P. Li, J. Zhou, G. Cheng, S. Chen, W. Luo, *ACS Catal.* **2019**, 9, 3744; b) L. Chen, Y. Zhang, H. Wang, Y. Wang, D. Li, C. Duan, *Nanoscale* **2018**, 10, 21019.

[27] a) T. Tang, W.-J. Jiang, S. Niu, N. Liu, H. Luo, Y.-Y. Chen, S.-F. Jin, F. Gao, L.-J. Wan, J.-S. Hu, *J. Am. Chem. Soc.* **2017**, 139, 8320; b) S. Zhao, R. Jin, H. Abroshan, C. Zeng, H. Zhang, S. D. House, E. Gottlieb, H. J. Kim, J. C. Yang, R. Jin, *J. Am. Chem. Soc.* **2017**, 139, 1077.

[28] H.-Y. Wang, S.-F. Hung, H.-Y. Chen, T.-S. Chan, H. M. Chen, B. Liu, *J. Am. Chem. Soc.* **2016**, 138, 36.

[29] Y. Shi, B. Zhang, *Chem. Soc. Rev.* **2016**, 45, 1529.

[30] B. H. Solis, S. Hammes-Schiffer, *J. Am. Chem. Soc.* **2011**, 133, 19036.

[31] J. Tian, Q. Liu, A. M. Asiri, X. Sun, *J. Am. Chem. Soc.* **2014**, 136, 7587.

[32] B. Sidhureddy, J. S. Dondapati, A. Chen, *Chem. Commun.* **2019**, 55, 3626.

[33] J. Liu, Y. Gao, X. Tang, K. Zhan, B. Zhao, B. Y. Xia, Y. Yan, *J. Mater. Chem. A* **2020**, 8, 19254.

[34] L. Yan, L. Cao, P. Dai, X. Gu, D. Liu, L. Li, Y. Wang, X. Zhao, *Adv. Funct. Mater.* **2017**, 27, 1703455.

[35] N.-T. Suen, S.-F. Hung, Q. Quan, N. Zhang, Y.-J. Xu, H. M. Chen, *Chem. Soc. Rev.* **2017**, 46, 337.

[36] a) R. Zhang, X. Ren, S. Hao, R. Ge, Z. Liu, A. M. Asiri, L. Chen, Q. Zhang, X. Sun, *J. Mater. Chem. A* **2018**, 6, 1985; b) Z. Wang, H. Liu, R. Ge, X. Ren, J. Ren, D. Yang, L. Zhang, X. Sun, *ACS Catal.* **2018**, 8, 2236.

[37] L. Su, X. Cui, T. He, L. Zeng, H. Tian, Y. Song, K. Qi, B. Y. Xia, *Chem. Sci.* **2019**, 10, 2019.

[38] a) Z. Wang, S. Wang, L. Ma, Y. Guo, J. Sun, N. Zhang, R. Jiang, *Small* **2021**, 17, 2006770; b) A. Kondori, M. Esmaeilirad, A. Baskin, B. Song, J. Wei, W. Chen, C. U. Segre, R. Shahbazian-Yassar, D. Prendergast, M. Asadi, *Adv. Energy Mater.* **2019**, 9, 1900516; c) S. Chu, W. Chen, G. Chen, J. Huang, R. Zhang, C. Song, X. Wang, C. Li, K. Ostrikov, *Appl. Catal. B: Environ.* **2019**, 243, 537; d) L. Yan, B. Zhang, S. Wu, J. Yu, *J. Mater. Chem. A* **2020**, 8, 14234.

[39] a) H. Ge, G. Qi, E.-T. Kang, K. G. Neoh, *Polymer* **1994**, 35, 504; b) T. Gao, Z. Jin, Y. Zhang, G. Tan, H. Yuan, D. Xiao, *Electrochim. Acta* **2017**, 258, 51.

Figures

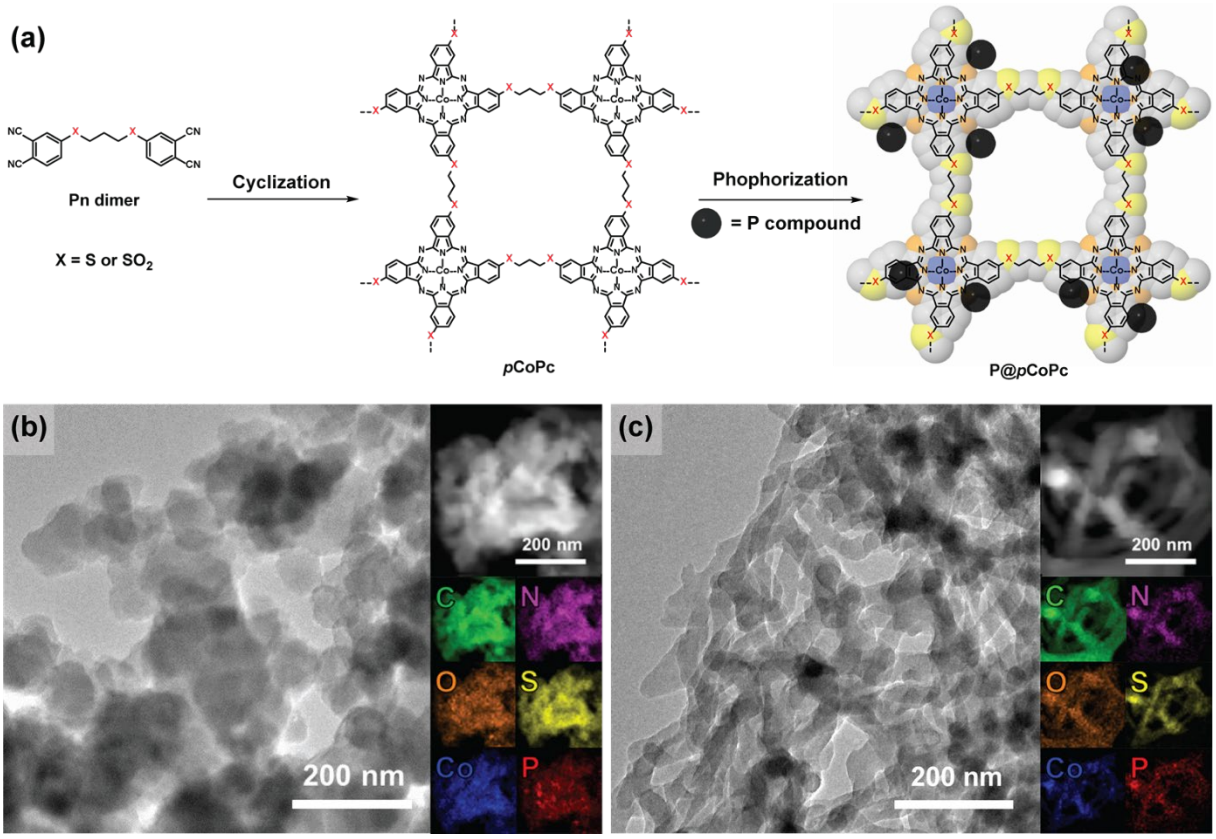

Figure 1. (a) Schematic illustration of ***p*CoPc** and **P@*p*CoPc** synthesis. TEM and the corresponding EDS mapping images of **P@*p*CoPc-1** synthesized by (b) a conventional method and (c) a solvothermal method.

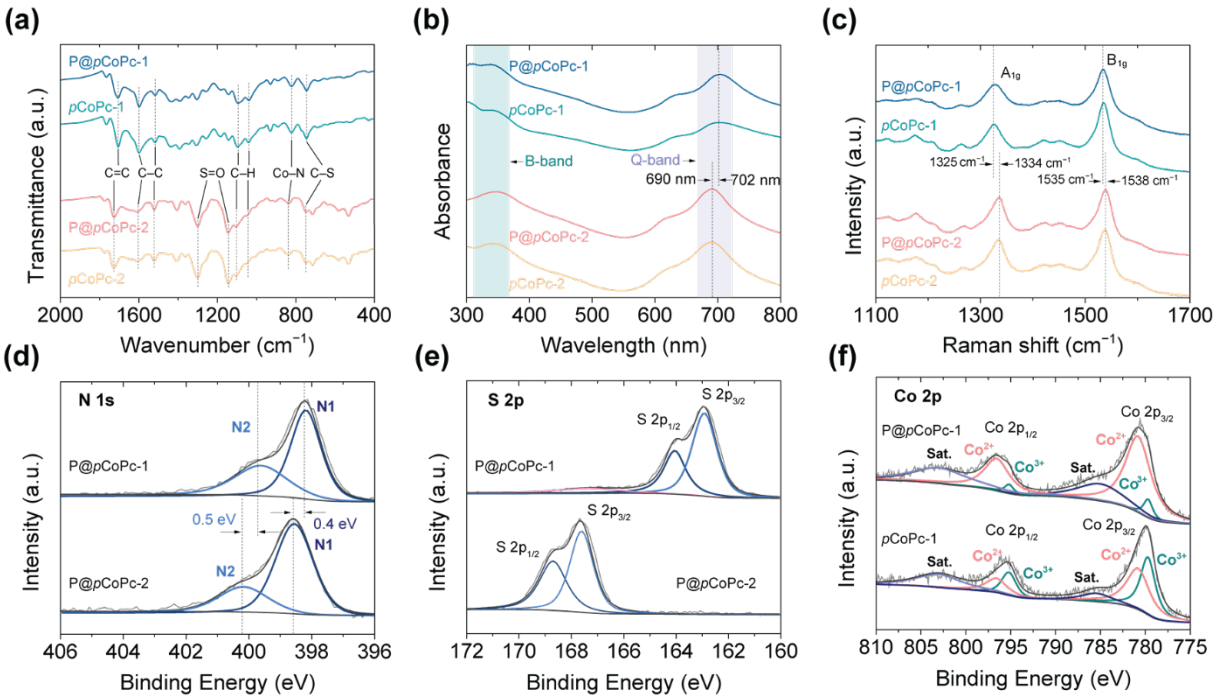

Figure 2. (a) FT-IR, (b) UV–vis, and (c) Raman spectra of ***p*CoPc-1**, ***p*CoPc-2**, **P@*p*CoPc-1**, and **P@*p*CoPc-2**. High-resolution XPS spectra of **P@*p*CoPc-1** and **P@*p*CoPc-2** in (d) N 1s and (e) S 2p regions. (f) High-resolution Co 2p XPS spectra of **P@*p*CoPc-1** and ***p*CoPc-1**.

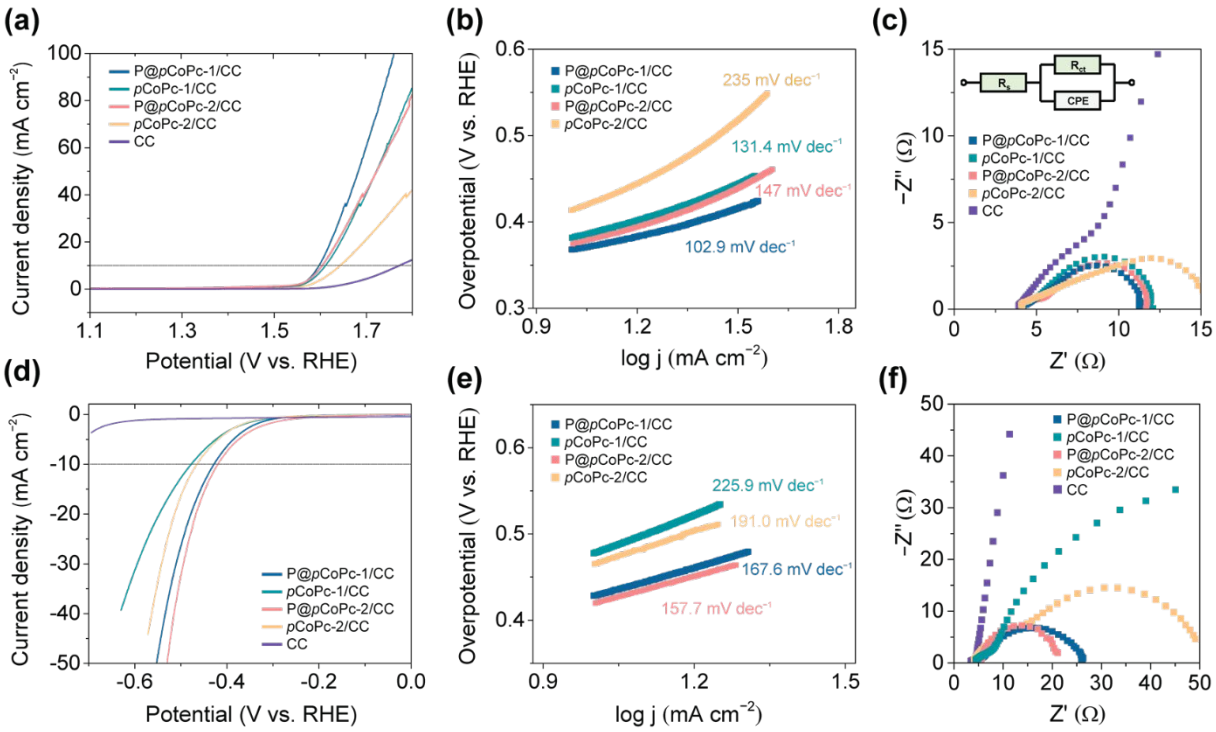

Figure 3. (a, d) LSV curves, (b, e) Tafel plots, and (c, f) EIS spectra of the as-prepared catalysts on CC measured in 1.0 M KOH. (a–c) for OER; (d–f) for HER. Inset in (c) is the equivalent circuit used for EIS data analysis in this work.

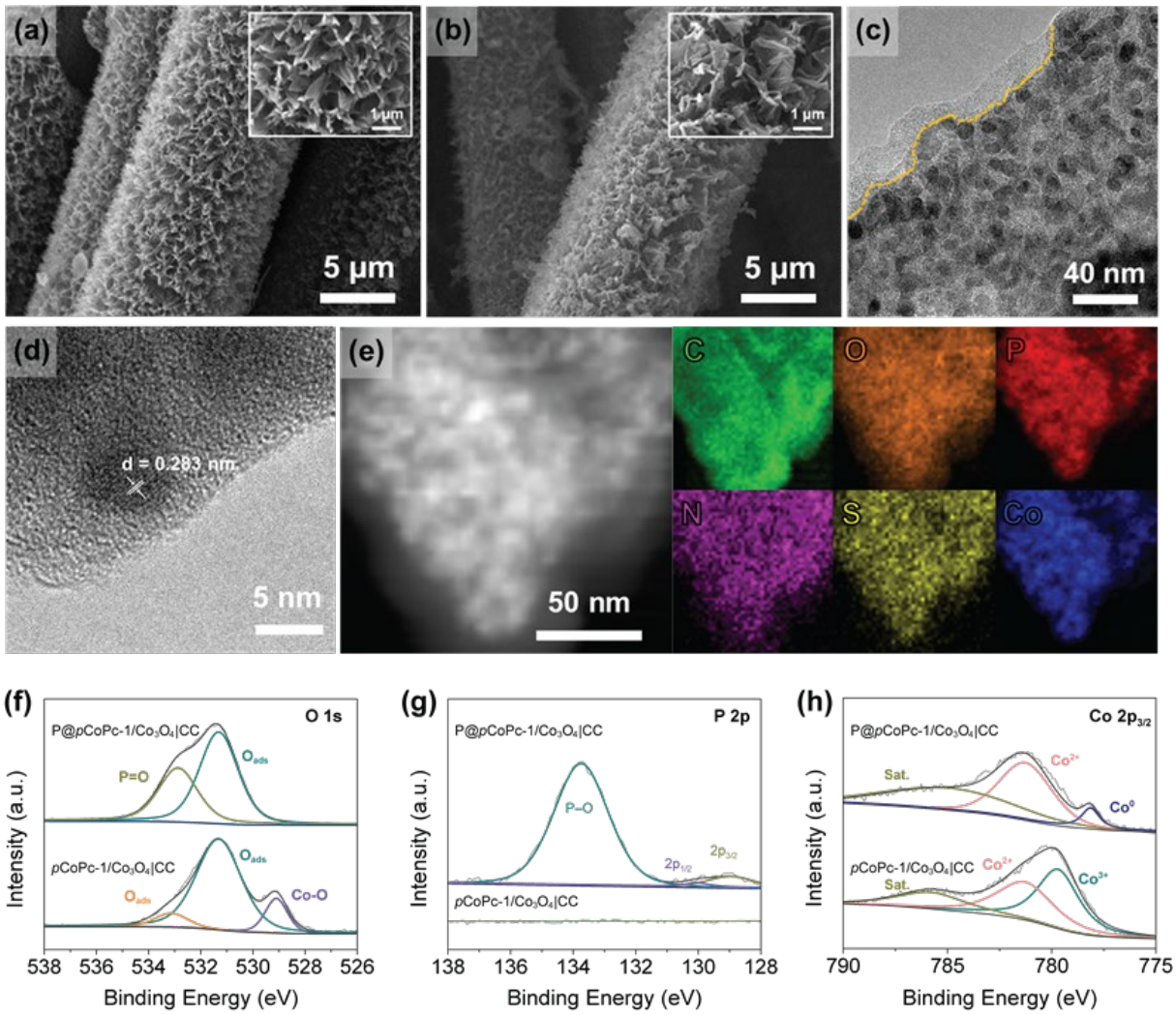

Figure 4. SEM and high-magnification SEM (inset) images of (a) ***p*CoPc-1/Co$_3$O$_4$|CC** and (b) **P@*p*CoPc-1/Co$_3$O$_4$|CC**. (c) TEM image and (d) HRTEM image of **P@*p*CoPc-1/Co$_3$O$_4$|CC**. (e) EDS mapping images of **P@*p*CoPc-1/Co$_3$O$_4$|CC**. High-resolution XPS spectra of **P@*p*CoPc-1/Co$_3$O$_4$|CC** and ***p*CoPc-1/Co$_3$O$_4$|CC** in (f) O 1s, (g) P 2p, and (h) Co 2p$_{3/2}$ regions.

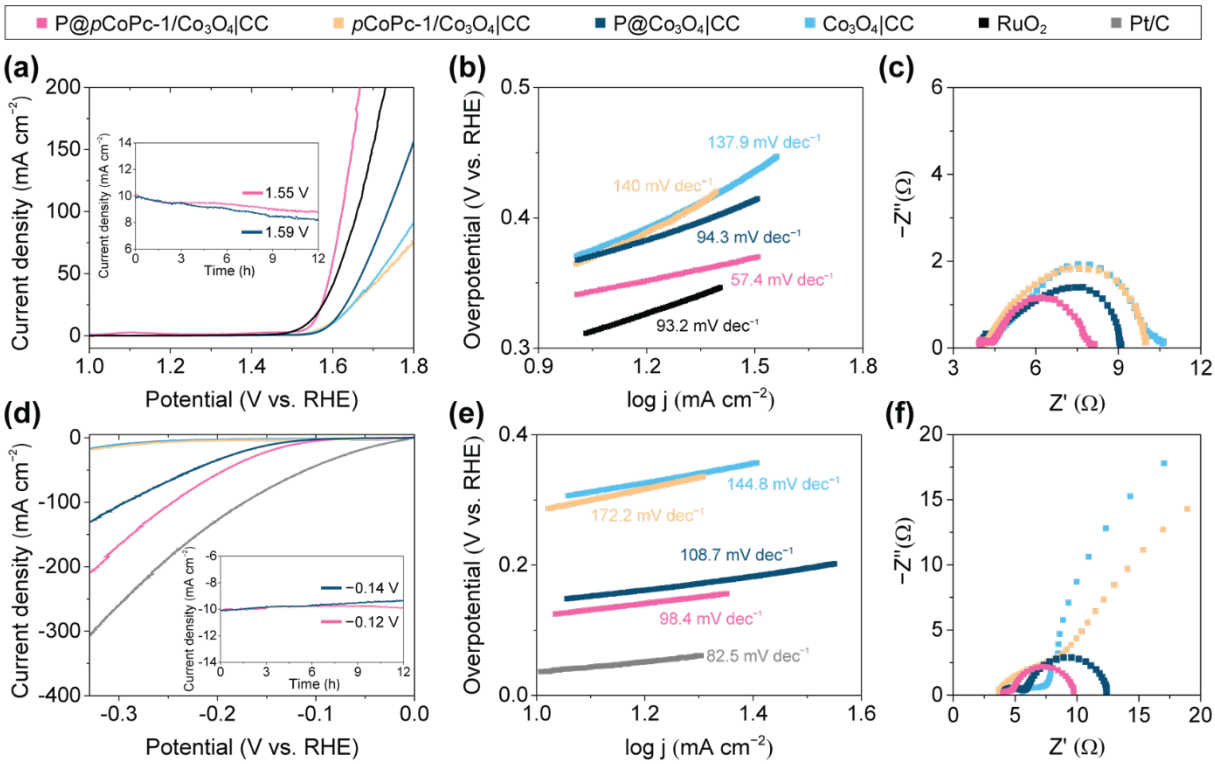

Figure 5. (a, d) LSV curves, (b, e) Tafel plots, and (c, f) EIS spectra of **P@*p*CoPc-1/Co$_3$O$_4$|CC**, ***p*CoPc-1/Co$_3$O$_4$|CC**, **P@Co$_3$O$_4$|CC**, and **Co$_3$O$_4$|CC** measured in 1.0 M KOH. (a–c) for OER; (d–f) for HER. Insets in (a) and (c) are the *i*-t curves at constant overpotentials.

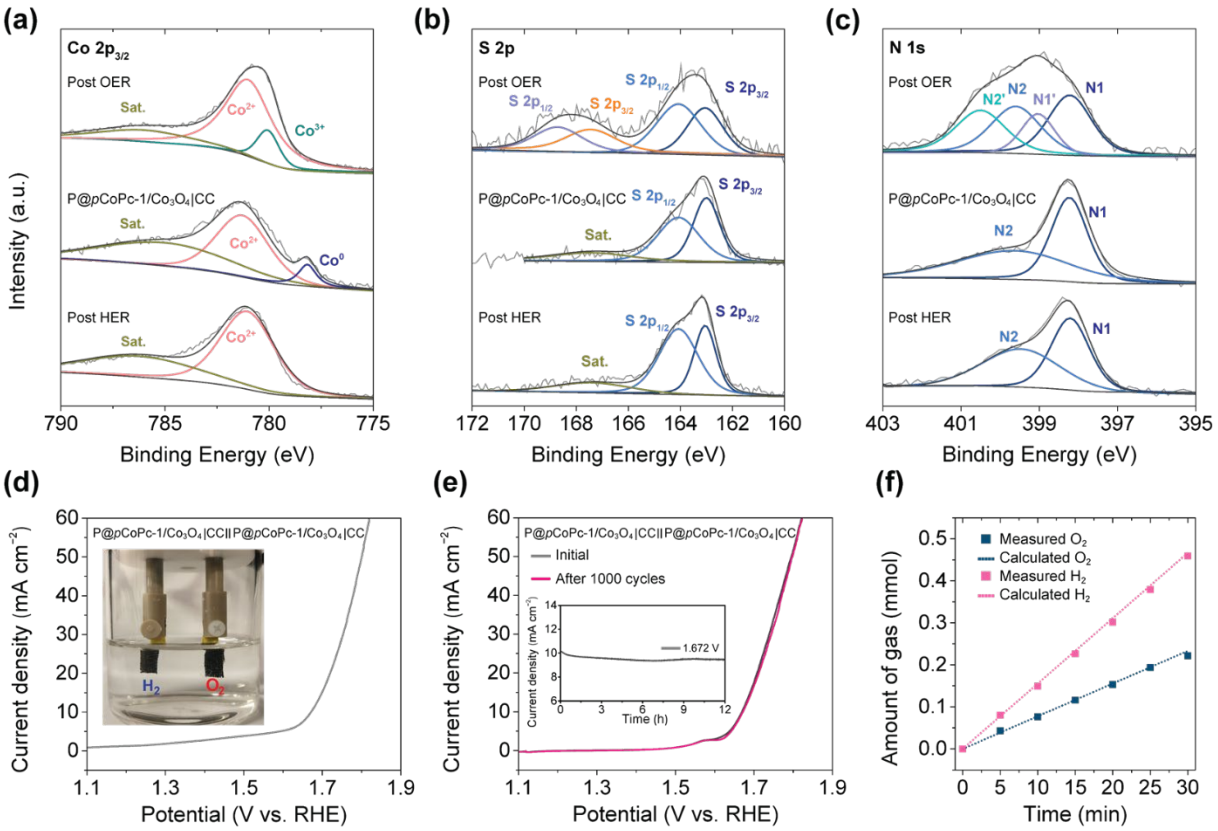

Figure 6. High-resolution XPS spectra in (a) Co $2p_{3/2}$, (b) S 2p, and (c) N 1s regions of **P@*p*CoPc-1/Co$_3$O$_4$|CC** after OER and HER. LSV curve of **P@*p*CoPc-1/Co$_3$O$_4$|CC** electrolyzer (d) during overall water splitting and (e) before and after 1,000 cycles. Insets in (d) and (e) are the setup for overall water splitting and the *i*-t curves of the chronoamperometric test at 1.672 V for 12 h, respectively. (f) The measured and calculated amounts of H_2 and O_2 as a function of time during the overall water splitting at a current density of 50 mA cm^{-2}.